Applied Geochemistry 161 (2024) 105835

Contents lists available at ScienceDirect

Applied Geochemistry

journal homepage: www.elsevier.com/locate/apgeochem

Control of brine composition over reactive transport processes in calcium carbonate rock dissolution: Time-lapse imaging of evolving dissolution patterns

Priyanka Agrawal [a,*], Hamed Aslannejad [a], Arjen Mascini [b], Tom Bultreys [b], Amir Raoof [a], Veerle Cnudde [a,b], Ian B. Butler [c], Mariëtte Wolthers [a,**]

[a] Department of Earth Sciences, Utrecht University, Utrecht, Netherlands
[b] PProGRess/UGCT, Department of Geology, Ghent University, Ghent, Belgium
[c] School of Geosciences, University of Edinburgh, Edinburgh, UK

ARTICLE INFO

Editorial handling by: Michael Kersten

Keywords:
Carbonate dissolution
Micro-CT
Reactive transport
Acid well stimulation
Wormhole formation
Porosity-permeability relation

ABSTRACT

This study investigates the impact of brine composition—specifically calcium ions and NaCl-based salinity—on the development of dissolution features in Ketton, a porous calcium carbonate rock. Utilizing a laboratory XMT (X-ray microtomography) scanner, we captured time-lapse *in situ* images of Ketton samples throughout various dissolution experiments, conducting four distinct flow-through experiments with differing brine solutions at a flow rate of 0.26 ml min^{-1}. The scans yielded a voxel size of 6 μm, enabling the assessment of the temporal evolution of porosity and pore structure through image analysis and permeability evaluations via single-phase fluid flow simulations employing direct numerical solutions and network modeling, as opposed to direct measurement.

Time-lapse imaging technique has delineated the extent to which the concentrations of $CaCl_2$ and NaCl in the injecting solution control the structural evolution of dissolution patterns, subsequently triggering the development of characteristic dissolution pattern. The inflow solution with no Ca^{2+} ions and with the minimal salt content manifested maximum dissolution near the sample inlet, coupled with the formation of numerous dissolution channels, i.e., wormholes. Conversely, solutions with a trace amount of Ca^{2+} ions induced focused dissolution, resulting in the formation of sparsely located channels. Inflow solutions with high concentrations of both Ca^{2+} ions and salt facilitated uniformly dispersed dissolution, primarily within microporous domains, initiating particle detachment and displacement and leading to localized pore-clogging. The relative increase in permeability, in each experiment, was correlated with the developed dissolution pattern. It was discerned that varying ratios of salt and calcium concentrations in the injected solution systematically influenced image-based permeability simulations and porosity, allowing for the depiction of an empirical porosity-permeability relationship.

1. Introduction

Carbonate formations constitute ~20% of sedimentary basins and ~60% of the world's hydrocarbon reservoirs (Morse and Mackenzie, 1990; Akbar et al., 2000; Schlumberger, 2019) and calcite is the dominant mineral in these reservoirs. Applications such as CO_2 sequestration or acid stimulation for enhanced oil and gas production from carbonate reservoirs involve the interaction of an acidic fluid with the calcite. This leads to the dissolution of calcite and the creation of secondary porosity and permeability.

Numerous studies have shown that parameters such as injection rate, the acidity of the injected solution, and initial heterogeneity of the porous medium can impact the dissolution processes and control the subsequent evolution of rock properties (e.g., Esteves et al., 2020; Golfier et al., 2002; Hoefner and Fogler, 1988; Luquot and Gouze, 2009; Meile and Tuncay, 2006; Menke et al., 2017; Soulaine et al., 2017; Yoo et al., 2021). In particular, dissolution kinetics along with the acid injection rate is known to form characteristic dissolution pattern (e.g.,

* Corresponding author.
** Corresponding author.
E-mail addresses: p.agrawal@uu.nl (P. Agrawal), m.wolthers@uu.nl (M. Wolthers).

https://doi.org/10.1016/j.apgeochem.2023.105835
Received 6 January 2021; Received in revised form 30 September 2023; Accepted 7 November 2023
Available online 24 November 2023

Daccord et al., 1993; Elkhoury et al., 2013; Golfier et al., 2002; Hoefner et al., 1987; Hoefner and Fogler, 1988; Luquot et al., 2014; Luquot and Gouze, 2009; Maheshwari et al., 2013; Panga et al., 2005). At the pore scale, the interaction of an acid with calcite mineral is a combination of two processes: (i) the transport rate of the aqueous ions to and from the mineral surface and (ii) the dissolution reaction taking place at the mineral surface. Manipulation of the rate of any of these processes affects the effective dissolution rate and consequently the dissolution patterns. In general, five types of dissolution patterns have been reported, corresponding to different dissolution kinetics for a given acid injection rate (e.g., Fredd and Fogler 1998; Hoefner and Fogler, 1988; Maheshwari et al., 2013; Soulaine et al., 2017): 1) face dissolution, 2) conical wormholes, 3) dominant wormholes, 4) ramified wormholes, and (5) uniform dissolution. For example, when the injected solution is highly reactive such that the transport time scale of the acid is longer compared to the reaction time scale of the acid, the acid is mostly consumed to dissolve the rock close to its inlet face. This leads to the development of the face dissolution pattern. Acid solutions with low reactivity, on the other hand, can penetrate further into the rock, causing uniform dissolution since time scale of transport becomes smaller than the time scale of chemical reaction. In summary, with decrease in the dissolution rate, the dissolution regime changes from the face dissolution regime to the uniform dissolution regime, while passing through the intermediate regimes corresponding to the different wormhole dissolution patterns. These patterns have a major control on the required amount of acid volume that needs to flow through the sample to achieve specific permeability increase for the same amount of porosity increment (e.g., Fredd and Fogler 1998; Hoefner and Fogler, 1988; Maheshwari et al., 2013; Soulaine et al., 2017; Yoo et al., 2021). For example, among the five dissolution patterns, the dominant wormholes are the most conducting channels and require the least volume of acid injection to enhance the permeability by a certain amount.

One way of controlling which dissolution regime is achieved in reactive-transport dissolution is by addition of dissolution-inhibiting or -enhancing compounds. Examples are the addition of microemulsion (Hoefner et al., 1987), varying the CO_2 concentration (Luquot et al., 2014) or using SO_4^{2-} ions in the injected acid Garcia-Rios et al. (2015); Luquot et al. (2014) showed that high pCO_2 developed preferential flow paths while lower pCO_2 resulted in uniform dissolution. Garcia-Rios et al. (2015) observed the inhibitory effect of SO_4^{2-} ions on calcite dissolution rates while observing no significant effect on the created dissolution patterns.

The impact of salinity and dissolution-inhibiting or -enhancing ions and compounds present in formation water on pore geometry evolution during dissolution of porous carbonate rocks is less well-known. Hanor (1994) reported that the salinities of pore waters in subsurface basins may span over five orders of magnitude i.e., from few mg l^{-1} in shallow meteoric systems to over 400000 mg l^{-1} in evaporite-rich sedimentary basin such as Michigan Basin, in USA. Moreover, in the formation brines, Ca^{2+} is the second most abundant cation after Na^{+}. The concentration of Ca^{2+} can even exceed the Na^{+} concentration in formation waters with salinities higher than 300000 mg l^{-1} (Gledhill and Morse, 2006). Therefore, understanding the geochemistry of high salinity and Ca^{2+} rich formation waters is important in the assessment of (the permeability evolution in) carbonate minerals enriched sedimentary basins for applications such as CO_2 sequestration or acid stimulation for enhanced oil production.

Several batch dissolution experiments have examined the influence of the salinity of the solution and Ca^{2+} concentration on the calcite dissolution rates (Anabaraonye et al., 2019; Buhmann and Dreybrodt, 1987; Finneran and Morse, 2009; Gledhill and Morse, 2006; Gutjahr et al., 1996; Pokrovsky et al., 2005; Sjöberg and Rickard, 1985). For transport-controlled dissolution regime, no impact of the NaCl-based ionic strength on calcite dissolution rates is observed when $I < 1$ M (Pokrovsky et al., 2005), while strong inhibition of calcite dissolution rates is observed with NaCl-salinity >1 M (Gledhill and Morse, 2006). The impact of Ca^{2+} ions in solution on the dissolution rate is contested in literature. Some authors found that calcium inhibits calcite dissolution in neutral to basic conditions only (Sjoberg and Rickard, 1985), while others found that calcium ions enhance calcite dissolutions rates (Gutjahr et al., 1996; Gledhill and Morse 2006).

While there is a clear, albeit incoherent, impact of calcium and salinity on calcium carbonate dissolution rates, the implication of this influence on the development of secondary porosity and permeability in carbonate rocks is unknown. We are not aware of any reactive flow experimental studies that have explored the control of NaCl and Ca^{2+} concentration on the dissolution patterns.

Through time-lapse imaging, we have examined the influence of the amount of NaCl and Ca^{2+} ions in the injected solution over the structural evolution of dissolution patterns and subsequent development of characteristic dissolution pattern in Ketton samples. We present the results of four flow experiments using different acidic solutions with constant flow rate into four samples of oolitic limestone. The composition of these solutions, i.e., amount of salt and Ca^{2+} ions, was chosen to cover a wide range of dissolution kinetics. X-ray microtomography (XMT) image analysis and effluent analysis were used to calculate the removed mass of calcite and consequent changes in the porosity of the samples. The link between dissolution and permeability enhancement of the samples was investigated using numerical simulation of single-phase flow using two approaches: pore network modelling (PNM) approach utilizing the pore network extracted from the XMT images and direct numerical simulation (DNS) method, also utilizing the XMT images. Finally, for each experiment, development in permeability was related to the modified porosity of the sample.

2. Material and methods

For this study, we have utilized a relatively homogeneous carbonate rock type: Ketton limestone. This oolitic limestone is a part of the Lincolnshire Formation, which was deposited around 165 million years ago. Four cylindrical shape samples named K1, K2, K3, and K4, of 6 mm in diameter and ~12 mm in length were drilled side by side out of a limestone block. Calcite-equilibrated solutions were prepared using deionized water at an atmospheric pressure and room temperature conditions. The composition of these solutions calculated using PHREEQC (Parkhurst and Appelo, 2013) and Pitzer database is provided in Table S1. The samples were pre-saturated using a protocol based on that of Boone et al. (2014) outside of the flow cell under vacuum condition with a calcite-equilibrated solution for about 48 hrs. After mounting the pre-saturated sample in the flow cell, any air still present in the sample was flushed by flowing the calcite-equilibrated solution through the sample for ~2000 pore volumes at three flow rates, 10 ml min^{-1}, 5 ml min^{-1} and 1 ml min^{-1}. Then an image was taken to visually verify that no air was present within the sample and the full saturation of the pore space was achieved. To impose a uniform radial fluid at the injection face of the sample, an inert porous sintered glass plug (Robu glass por 0 filter) was placed in front of the inlet side of the carbonate plug. Both plugs were inserted into a Viton sleeve, placed in a custom-built Hassler-type flow cell made from X-ray transparent PEEK. A confining pressure of ~20 bar was applied on the sleeve to avoid fluid bypassing the sample. The fit of the sleeve to the sample was assessed visually on the raw data and was observed to fit very tightly (Fig. S1). Additionally, the confinement pressure meter indicated a consistent pressure of ~20 bar during the experiment, indicating a leak-free flow.

Note that flow was established from bottom to top of the sample while all presented images in the subsequent sections are upside down. All experiments were performed under room temperature and a confining pressure of ~20 bars.

2.1. Chemical composition of injecting solutions

Four solutions with the same HCl concentration of 0.001 mol dm^{-3}

but different salinity and Ca^{2+} concentration was prepared. All solutions were prepared by adding the appropriate amount of the reagents with, $CaCl_2$, NaCl, and HCl to deionized water under atmospheric conditions. pH values of these solutions are provided in Table 1. The first solution had an ionic strength of 0.2 mol dm^{-3}, without calcium ions (referred to as no calcium low salinity solution, or NCLS). A second solution had a similar ionic strength but contained 1×10^{-3} mol dm^{-3} of Ca^{2+} ions (low calcium low salinity solution, or LCLS). The third type of solution had an ionic strength of 1.2 mol dm^{-3}, without calcium ions (no calcium high salinity solution, or NCHS). Finally, the fourth solution had a similar ionic strength as the third but contained 0.335 mol dm^{-3} of Ca^{2+} ions (high calcium high salinity solution, or HCHS). For all four experiments, acidic solutions were injected with a same and constant flow rate of 4.16×10^{-9} m^3s^{-1} (i.e., Q = 0.26 ml min^{-1}).

The concentration of Ca^{2+} ions in inflow and outflow solutions was measured with the ICP-OES method. This method can measure Ca^{2+} concentration within a range of 0.5-5 $\times 10^{-3}$ mol dm^{-3}. Therefore, most of the solutions were diluted using 0.7 M HNO_3 acid, to a dilution ratio of 1:100, while some of the solutions related to experiment HCHS were diluted by a ratio of 1:1000. The pH of the original inflow and outflow solutions (i.e., without dilution) was measured with a pH 3110 portable pH meter and pH electrode SenTix™ or (for the HCHS experiment) WTW - Sensolyt 900-P.

The solution composition of all inflow solutions was calculated using PHREEQC (Parkhurst and Appelo, 2013) with the Pitzer database. These calculations showed that the activity coefficient of H^+ is close to unity for all solutions (Table S1). For inflow solutions NCLS and LCLS, the measured value of pH matched with the calculated value of pH. It should be noted that the measured pH values for the NCHS and the HCHS was affected by the non-compatibility of the utilized electrode with the high concentration of ions in the solutions. As a consequence, the measured value of pH of these solutions using above mentioned electrode differed from the calculated value of pH. In order to clarify the uncertainties over pH values, we have re-measured pH with a different pH electrode WTW - Sensolyt 900-P and multimeter WTW portable pH meter Multiline Multi 3630 IDS. These measurements were performed on a separate solution prepared with the same recipe as that of the inflow solution for experiment HCHS. A measured pH value of 3.03 for this solution using pH electrode WTW - Sensolyt 900-P further affirms the non-compatibility of the pH electrode SenTix™ for measurements in high salt (calcium and chloride) solutions. Table 1 summarizes experimental details related to flow and solution chemistry. Note that the Pitzer model is not tailored to the exact conditions at the start of, and during our experiments. Therefore, the SI's calculated for calcite (Table 1) should be treated with

Table 1
Parameters for all four dissolution experiments including the skeleton (pore network) information.

Experiment	NCLS	LCLS	NCHS	HCHS	Method
Ketton sample	K1	K2	K3	K4	–
Flow rate (m^3s^{-1})	4.16×10^{-9}	4.16×10^{-9}	4.16×10^{-9}	4.16×10^{-9}	–
Darcy velocity (m s^{-1})	1.54×10^{-4}	1.54×10^{-4}	1.54×10^{-4}	1.54×10^{-4}	–
Injection duration (s)	72000	72000	43200	57000	–
Injected pore volume	6722	6977	3507	4489	–
Inflow pH(Calculated)	3.1	3.1	3.00	3.05	PHREEQC Pitzer
Inflow pH (Measured)	3.01	2.97	2.77	3.03[c]	pH electrode SenTix™or WTW
Inflow Ca^{2+} (mol dm^{-3})	–	1×10^{-3}	–	335×10^{-3}	ICP-OES
Inflow -salinity (mol dm^{-3})	0.2×10^{-3}	0.2×10^{-3}	1.16×10^{-3}	1.12×10^{-3}	ICP-OES
Inflow-saturation index (SI)	–	−11.45	–	−8.04	PHREEQC Pitzer
Porosity at t = 0s (%)	13.42	12.1	13.88	16.3	XMT[a]
Permeability (k_{PNM}) at t = 0s (m^2)	1.13×10^{-12}	6.37×10^{-13}	1.31×10^{-12}	3.18×10^{-12}	Flow simulation on cropped sample length using PNM
Permeability (k_{DNS}) at t = 0s (m^2)	1.98×10^{-12}	4.75×10^{-12}	1.77×10^{-12}	3.97×10^{-12}	Flow simulation on cropped sample length using DNS
Average equivalent diameter at t = 0s (m)	0.89×10^{-4}	0.53×10^{-4}	0.51×10^{-4}	0.65×10^{-4}	XMT[a]
Average volume of pores at t = 0s (m^3)	0.57×10^{-11}	0.29×10^{-11}	0.31×10^{-11}	0.47×10^{-11}	XMT[a]
Number of pores in the extracted pore network	6832	6259	6948	6130	PNM[b]
Number of throats in the extracted pore network	12419	10915	12919	10919	PNM[b]
Average pore radius at t = 0s (m)	5.46×10^{-5}	4.97×10^{-5}	4.93×10^{-5}	5.31×10^{-5}	PNM[b]
Average throat radius at t = 0s (m)	2.59×10^{-5}	2.61×10^{-5}	2.59×10^{-5}	2.93×10^{-5}	PNM[b]
Average coordination number at t = 0s	3.64	3.49	3.72	3.56	PNM[b]
Average pore velocity at t = 0s (m s^{-1})	2.43×10^{-5}	2.79×10^{-5}	2.47×10^{-5}	2.47×10^{-5}	PNM[b]
Size of the full sample length (Voxels)	1319 × 1317 × 2494	1316 × 1316 × 2418	1317 × 1319 × 2552	1317 × 1318 × 2342	XMT Images
Size of the cropped sample length (Voxels)	1319 × 1317 × 1950	1316 × 1316 × 1950	1317 × 1319 × 1950	1317 × 1318 × 1850	XMT Images
Size of the half sample length (Voxels)	1319 × 1317 × 818	1316 × 1316 × 850	1317 × 1319 × 850	1317 × 1318 × 782	XMT Images
Scan interval of the half sample length (min)	40,136, 154, 154, 154, 154, 154	90, 90, 90, 99, 105, 120, 126	150,30,180,120,120,160,136,56	40,215,20,75,165,165,165,165,165,25	–

[a] XMT image of cropped sample length.
[b] Pore Network Model of cropped sample length.
[c] pH measurements were done on a separate solution made according to the same recipe and using a WTW – Sensolyt 900-P pH electrode; for this solution, the SenTix electrode was affected by the high concentration of ions in the solutions.

caution.

2.2. Data acquisition and processing

In situ imaging of the sample was performed using a laboratory-based environmental micro-CT scanner built at Ghent University (Bultreys et al., 2016). The starting step of each experiment was the saturation of the sample with calcite-equilibrated water, followed by scanning of the sample. The scanning was performed with an X-ray beam energy of 110 kV and an exposure time of 80ms. The reconstructed voxel size of the images was 6 μm per voxel and three stacks were required to cover the full length of the sample. Such full sample length scanning was performed at the beginning and the end of the experiment. During acid injection, the scanner was fixed near the inlet of the sample; therefore, time-lapse scans correspond to the top ~6 mm section of the sample. Hereafter, these time-lapse scans are referred as half-length sample volumes. For both full-length scans and half-length scans, a total of 2200 projections, covering a 360° rotation of the scanner, were obtained in 15 min. Details on the processing steps of both types of scans is provided in SI Section 1.

2.3. Skeleton analysis

In this study, we used the skeletonization methods to characterize the wormholes created during limestone dissolution. The skeletonization workflow converts the three-dimensional pore space into a one-dimensional object while preserving topological and geometrical features. This process of dimension reduction includes iterative removal of individual voxels from a volume until a single line of voxels (i.e., the medial axis of the volume) remains along the pore space. This yields a simplified skeleton representation of the pore space, in which each voxel stores properties of the original complex 3D pore space through attributes like thickness, orientation and length. Detailed steps on the skeletonization of wormholes and subsequent quantification of the wormhole are provided in SI Sections S2 and S3, respectively.

2.4. Pore network extraction and flow modelling

We have calculated the velocity field and permeability of the sample at a different stage of the dissolution process. For this purpose, we have utilized a pore network model because it requires less computational time than direct numerical simulation. Single phase flow was simulated on the extracted pore network. For simulating flow, the inlet face of the network was maintained at a constant value of Darcy velocity (i.e., constant average pore inlet velocity) and the outlet face at an atmospheric pressure condition, after which the pressure and velocity in each pore were found by imposing mass conservation. The Darcy velocity was calculated as:

$$u_D = \frac{Q}{A} \tag{1}$$

where, Q is the volumetric flow rate ($m^3\ s^{-1}$) and A is the cross-section area of the sample (m^2).

From the Darcy velocity (u_D) and pressure difference between the inlet and outlet faces (ΔP_{PNM}), the permeability of the network is obtained from:

$$k_{PNM} = \frac{\mu u_D L}{\Delta P_{PNM}} \tag{2}$$

where, μ is the viscosity of water, 0.001 Pa s, and L is the pore network length along the flow direction.

The remaining boundaries of the network parallel to the flow direction were implemented as no-flow boundaries. Further details on the modeled equations can be found in Raoof et al. (2012).

2.5. Direct flow simulation of pore-scale images

In order to evaluate the permeability changes during dissolution, XMT images which were acquired at the start and end of the experiment were used as 3D pore space domains for the microscale fluid flow simulation.

The XMT-based pore spaces were first simplified and scaled using open-source image processing software, MeshLab (MeshLab, version 2021.05; https://www.meshlab.net). The resulting pore space was used for fluid flow simulations under same flow direction as that of experiments. Flow equation were solved with a pressure difference imposed on either side of the sample and a no-slip boundary condition at the lateral faces of the domain.

OpenFOAM, an open-source CFD toolbox, was used to perform single phase flow simulation (Aslannejad et al., 2018; Bedram and Moosavi, 2011). For meshing purposes, a native meshing tool of OpenFOAM (in this case, snappyHexMesh) was used. The flow simulation required a significant number of discretization cells (i.e., base refinement level: 100 × 100 × 250); therefore, the parallel computation was done using 8-cores. Classic Semi-Implicit Method for Pressure Linked Equations (SIMPLE) algorithm was used to solve flow equation.

Absolute permeability, k_{DNS} (m^2) was calculated using the Darcy equation:

$$k_{DNS} = \frac{\mu\, Q L_x}{\Delta P_{DNS}\, L_y\, L_z} \tag{3}$$

where, Q ($m^3.s^{-1}$) is flow rate, L_x, L_y and L_z are the domain dimensions in each direction and ΔP_{DNS} is the imposed pressure difference. A mesh sensitivity study was performed by varying the number of discretization cells in the x, y, and z directions. Along with the base refinement level, two more refinement levels i.e., refinement level 1: 100 × 100 × 150 and refinement level 2: 200 × 200 × 250, were simulated. Cropped sample length-based dataset of Sample K1 belonging to the start and end of the experiment was utilized. We observed that a 4x increment in discretization cell numbers (base refinement level and refinement level 2) results in ~8% permeability variation for the unreacted rock volume and ~18% permeability variation for the dissolved rock volume, while the relative change in permeability due to dissolution is comparable among different mesh configurations (Fig. S2).

2.6. Sample characterization prior to experiments

Characterization of the Ketton samples is based on the XMT images, FIB-SEM images, EDS analysis, XRD analysis, and properties of the extracted pore networks.

XMT images showed that Ketton is composed of spherical grains and can be considered a relatively homogeneous carbonate rock at the macroscopic scale (Figs. S1 and S4). Electron microscopy imaging of the surface and cross-sectional view of a randomly chosen spherical grain were done using FIB-SEM imaging technique. Results showed the extent of the intra-grain porosity (Fig. S7). SEM images of the part of the sample showed textural heterogeneity at a microscopic scale (Fig. S8). We observed that some part of the grain was made of rhombohedral particles, which is a typical morphology of calcite. Other parts of the grain were made of needle-shaped particles, which is a typical morphology of aragonite (e.g. Nan et al., 2008). EDS analysis suggested that these particles were majorly composed of Ca, C and O (Fig. S9).

In order to identify the particle polymorph, we conducted XRD analysis of three new samples that were extracted from the same Ketton limestone block. Fig. S10 shows the cosmparison of the XRD spectra of a representative sample with the RRUFF reference of calcite, suggesting that Ketton is predominately composed of the calcite and that the needle-shaped particles are probably the pseudomorphs i.e., aragonite converted into calcite (Fig. S8).

Next, the petrophysical properties of the four samples i.e., K1, K2, K3

and K4 were investigated through analysis of the initial XMT images and of the extracted pore networks for the initial conditions in the samples. The initial porosity of each sample was calculated by dividing the volume of pore space by the total volume of the sample. The initial permeability of each sample was calculated from the single-phase flow simulation on extracted pore networks. A comparison of the porosity of all samples shows that K1, K2 and K3 have similar initial porosity while K4 has a different initial porosity (Table 1).

Fig. S11 shows the statistical distribution of some of the characteristic properties of the initial pore space of the samples. K1, K2 and K3 have similar throat radii and K2 and K3 have similar pore sizes. K4 has a slightly wider range of pore sizes and throat widths than K1–K3, while all four samples have a similar distribution of coordination numbers. Fig. S11e shows the frequency distribution of the normalized velocity which was obtained by normalizing the velocity value of each throat (i.e., obtained from PNM) by the Darcy velocity. The Darcy velocity was obtained by dividing the flow rate with the cross-sectional area of the sample. The frequency distribution of normalized velocity indicated the probability of faster and slower velocity channels in comparison with the Darcy velocity. K2 and K4 have a somewhat greater number of fast channels as compared to K1 and K3. The observed velocity field in this study is similar to the previously reported velocity field for Ketton samples (Al-Khulaifi et al., 2017). Overall, the narrowness of the velocity channel suggested that all four samples have relatively similar initial pore structure (Fig. S11e).

2.7. Quantification of the changed volume of calcite

$\Delta V^{n}_{Calcite,effluent}$, the cumulative value of changed amount of calcite volume (m^3), was obtained as:

$$\Delta V^{n}_{Calcite,effluent} = \frac{Q\, M_{calcite}}{\rho_{calcite}} \sum_{i=1}^{n} \Delta cCa^{i} \left(t^{i} - t^{i-1}\right) \tag{4}$$

where, n is the sampling steps, Q is the flow rate ($m^3\ s^{-1}$), $\rho_{calcite}$ is the density of calcite (2710 kg m^{-3}), $M_{calcite}$ is the molecular mass of calcite (0.1 kg mol^{-1}) and ΔcCa is the difference between outflow and inflow Ca^{2+} concentration (mol m^{-3}).

$\Delta V_{Calcite,XMT}$, the change in the number of solid voxels of XMT images in an experiment duration denoted by time t, is given as:

$$\Delta V_{Calcite,XMT} = V^{t}_{Calcite,XMT} - V^{t=0}_{Calcite,XMT} \tag{5}$$

Average reaction rate was calculated from the time-based evolution of the macroporosity as:

$$r_{calcite}(t) = \frac{\rho_{calcite}}{\Delta M_{calcite}} \frac{\Delta \varnothing_{XMT}(t)}{\Delta t} \frac{V_b}{A\,(t)} \tag{6}$$

where, $r_{calcite}(t)$ is the average reaction rate (mol $m^{-2}\ s^{-1}$), $\Delta\varnothing_{XMT}$ (t) is the change in the macroporosity of the sample between the scan time t as compared to the initial porosity, Δt (s) is the acquisition time of the image and A(t) (m^2) is the surface area obtained by adding up the voxel faces forming the boundary between solid and pore phase and V_b (m^3) is the total volume of the sample. It should be noted that above reaction rates are based only on macroporosity while neglecting the changes in the microporosity. Average reaction rates at different time steps of the experiment was calculated from the XMT images of the half-length sample. The average reaction rate at the beginning and at the end of the experiment was calculated from the XMT images of the cropped length sample. Note that the average reaction rate calculated from Equation (6) inherited an error depending on the time interval of scans used in the calculation (i.e., Δt). We observed that for the scan time interval used in this study, this error was around 20% (SI Section S4, Fig. S12).

Equation (6) calculates the average reaction rate from the average macroporosity changes. Additionally, we have calculated local reaction rate as:

$$rz_{calcite}(z) = \frac{\rho_{calcite}}{M_{calcite}} \frac{\Delta \varnothing_{XMT}(z)}{\Delta t} \tag{7}$$

where, $rz_{calcite}(z)$ is local reaction rate (mol m^{-3}) calculated from the change in the slice-averaged porosity of the sample (i.e., Fig. 4b) occurred in the experiment duration, Δt, and at a distance of z from the sample inlet.

In order to understand the coupling of transport and reaction times scales, we have defined two dimensionless numbers i.e., Peclet number and Damköhler number.

The Peclet number (Pe) compared the time scale of advection to that of diffusion and was defined as:

$$Pe(t) = \frac{U_{av}\,(t) l(t)}{D} \tag{8}$$

where, U_{av} (m s^{-1}) is the average pore velocity obtained by dividing constant Darcy velocity with the image-based porosity at different time steps, l is the mean pore radius calculated from the extracted pore network of the sample and D is the diffusion coefficient ($3.36 \times 10^{-9}\ m^2\ s^{-1}$).

The Damköhler number (Da) compared the convection time scale with the reaction time scale:

$$Da(t) = \frac{rz_{calcite}\, MV_{calcite}}{A U_{av}(t)} \tag{9}$$

where, $MV_{calcite}$ is the molar volume of calcite ($3.69 \times 10^{-5}\ m^3\ mol^{-1}$), $rz_{calcite}$ indicates the reactive strength of the injecting acid (mol $m^{-3}\ s^{-1}$) at the inlet of the sample calculated from Equation (7) and A is the specific surface area of the cropped sample length at the beginning of the experiment.

The Pe and Da number, at different time steps were calculated from the XMT data of the half sample length, while, at the beginning and at the end of the experiment were calculated from the XMT data of the cropped sample length.

3. Results and discussion

This study is based on four reactive flow experiments (Table 1 and Table S1): NCLS (No Calcium Low Salinity), LCLS (Low Calcium Low Salinity), NCHS (No Calcium High Salinity) and HCHS (High Calcium High Salinity). The analysis of effluent solution for all four experiments is provided in Section 3.1.1. The results are compared with the XMT image-based analysis in Section 3.1.2. Next, we assess the temporal evolution of bulk porosity and local porosity in Section 3.1.3 and corresponding effective reaction rate in Section 3.1.4. Further, we examine the characteristics of the dissolution structures developed in each experiment in Section 3.2. Finally, the impact of the dissolution structures on permeability changes is provided in Section 3.3.

3.1. Mass transfer analysis

3.1.1. Effluent analysis

Fig. 1a presents the temporal evolution of the normalized Ca^{2+} concentration (ΔcCa), which represents the difference between outflow and inflow Ca^{2+} concentration during the sampling interval. Positive values of ΔcCa for experiments NCLS, LCLS and NCHS indicates persisting dissolution throughout the experiments. From the first sampling point onwards, the experiment NCLS maintained a steady-state value of outlet Ca^{2+} concentration and ΔcCa. Experiment LCLS, on the contrary, initially provided a lower outflow concentration compared to NCLS, which later approach towards a higher steady-state value. For experiment NCHS, outflow Ca^{2+} concentration showed a decreasing trend. From the saturation index of the injected solutions, we estimated the maximum amount of Ca^{2+} concentration which could be dissolved

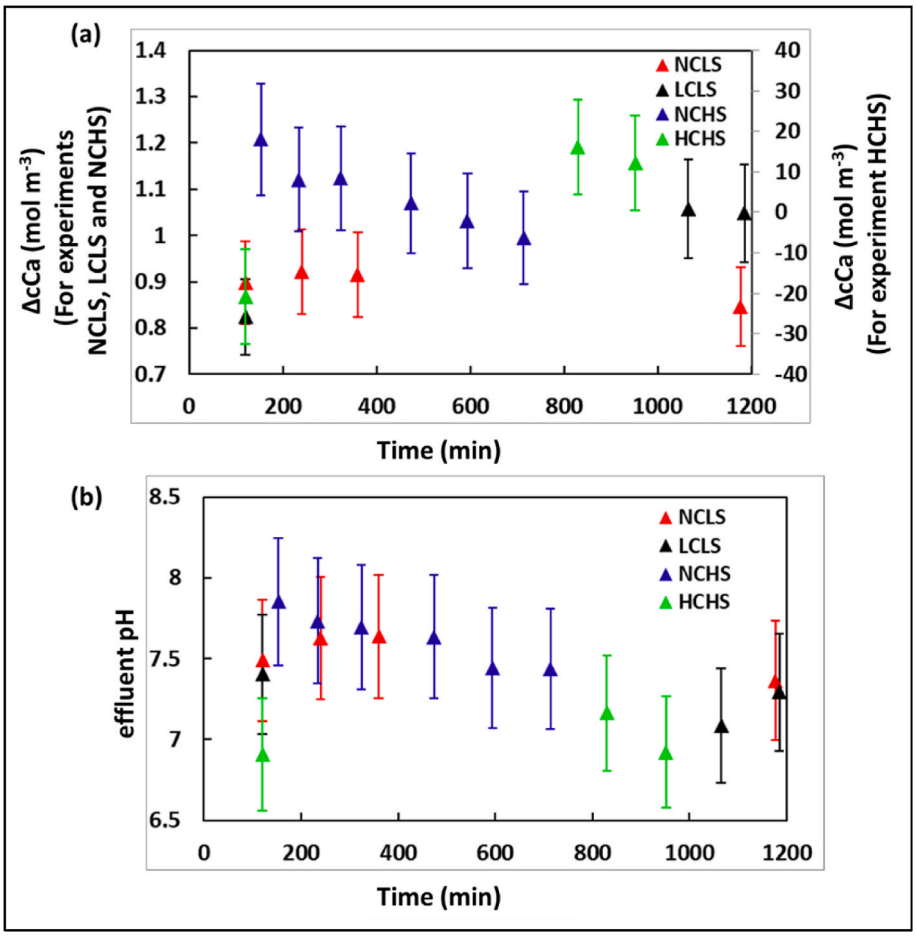

Fig. 1. (a) Measured Ca^{2+} concentrations from effluent solution for experiments NCLS, LCLS, NCHS (left-hand vertical axis) and HCHS (right-hand vertical axis) (b) Measured pH from effluent solution for all four experiments.

before these solutions would reach equilibrium with respect to calcite. Comparison of these estimates with the measured ΔcCa suggests that the outflow solutions of experiments NCLS, LCLS and NCHS were almost in equilibrium with calcite (Fig. 2a). Note that, the differences between the quantities of dissolved Ca^{2+} ions observed in the experiment and those in the simulation most likely reflect the impact of differences in sample's initial permeability on the overall amount of calcite dissolved during the experiments. Future investigations on homogenous porous media (e.g., 3D-printed) could circumvent such uncertainties.

In the case of experiment HCHS, normalized ΔcCa was negative initially, followed by positive values (Fig. 1a). As stated earlier, the inflow solution HCHS was acidic, with the measured pH value of 3.05, and undersaturated with respect to the calcite. Through the examination of mixing calculations (specifically, PHREEQC + Pitzer calculations when mixing varying fractions of inflow solution HCHS with a solution in equilibrium with calcite), we did not identify any ratios resulting in either supersaturated mixtures or salting-out conditions. Moreover, from the saturation index, we estimated that this solution can dissolve up to around 0.7×10^{-3} mol dm^{-3} calcite, before reaching equilibrium with respect to calcite (Fig. 2a). Therefore, it is most likely that the initial negative ΔcCa value does not represent calcite precipitation but was caused by error accumulation during the strong dilution necessary on in- and outflow samples in preparation of ICP-OES measurements from which ΔcCa values were calculated. We suspect the calculated Ca^{2+} concentrations for HCHS samples included an uncertainty larger than the standard error of 10% (SI Section S5.1, Fig. S13).

We observed the impact of salinity and Ca^{2+} concentration of the inflow solutions on the equilibrium concentrations (Fig. 2a). As expected, inflow solutions containing Ca^{2+} ions (i.e., LCLS and HCHS) required a lower amount of Ca^{2+} ions to reach to the equilibrium as compared to the inflow solutions with no Ca^{2+} ions (i.e., NCLS and NCHS) (Fig. 2a). Similarly, increments in salinity led to enhanced solubility of calcite, with more saline inflow solutions dissolving larger amounts of calcite than the inflow solutions with lower salinity (i.e., NCLS) (Fig. 2a).

Fig. 1b shows the measured pH of the effluent samples from all four experiments. Inflow solutions all had an approximate pH value of 3.0 (Table S1). The higher pH values measured in the outflow indicate dissolution-induced solution buffering. The amount of fluid buffering directly relates to the amount of Ca^{2+} ions produced (Fig. 1). Initially, experiment NCHS showed both the highest value of pH and Ca^{2+} concentration at the outflow, followed by a decreasing trend (Fig. 1). For experiment NCLS, outflow pH remained constant and for experiment LCLS, outflow pH showed an increasing trend. We observed a good agreement between the measured outflow pH and predicted outflow pH (Fig. 2b). For the experiment HCHS, the pH of the outflow solution was calculated corresponding to the equilibrium concentration. For this experiment, we observed a higher difference between the calculated pH and the measured pH (Fig. 2b). This is probably due to the higher uncertainty associated with the pH measurement in highly saline Ca^{2+}-rich outflow solution.

3.1.2. *Effluent concentrations vs XMT analysis*

The comparison of the calcium concentration in the effluent with ketton volume (loss) calculated from XMT image analysis helps to (further) quantify the amount of dissolution in the different

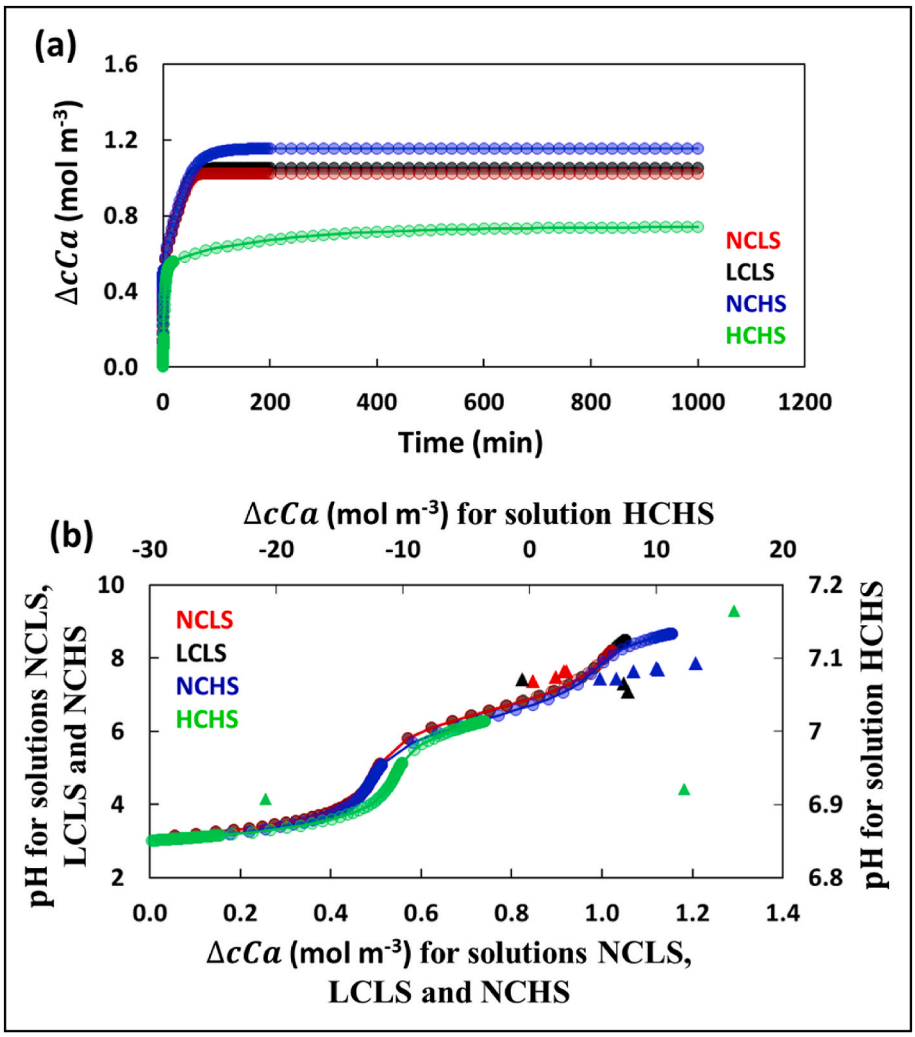

Fig. 2. PHREEQC simulations for all four injected solutions showing (a) the maximum amount of ΔcCa which can be dissolved before the solution reaches to the equilibrium and (b) pH of the solution as a function of the added amount of ΔcCa.

experiments. Fig. 3a shows a comparison of the changed amount of calcite volume, calculated using ΔcCa with values obtained from XMT image analysis using Equations (4) and (5), respectively. For experiments NCLS, LCLS and NCHS, we observed a difference of ~around 14–25% between values obtained from effluent analysis and those from XMT images (Fig. 3a). A potential cause of this discrepancy could be resolution of imaging (voxel size 6 μm). This difference would be dependent on the length of the sample along the flow direction used in volume change calculations. Increased difference for cropped length sample-based analysis, as shown in Fig. 3a, is due to dominance of dissolution close to the sample inlet. As discussed in Section 2.3, the remaining part of this study will be based on the analysis of the cropped length sample. Fig. S5 shows the cropping position through a vertical slice of sample K1. It should be noted that while the calculated mass of dissolved calcite from the effluent and XMT analyses doesn't exhibit an exact correspondence, they do, in essence, agree on the relative extent of dissolution rate among the NCLS, LCLS, and NCHS experiments.

For experiment HCHS, the difference between effluent analysis and XMT images was more significant (Fig. 3a). This, along with the arguments provided in Section 3.1 further suggests that the ICP-OES measurement of solutions containing a high amount of Ca^{2+} ions might have inherited higher uncertainty.

3.1.3. Porosity

The time-lapse imaging of the sample allowed *in situ* tracking and analysis of the dissolution-induced changes in the porosity. Fig. 3b shows the temporal evolution of macroporosity during the four experiments calculated from XMT images. Injection of undersaturated solutions led to an increase in the macroporosity of samples for experiments NCLS, LCLS, and NCHS. Consequently, total increments in the macroporosity are of magnitudes 0.025, 0.0296 and 0.0158 for experiments NCLS, LCLS, and NCHS, respectively. It should be noted that the observed reduction in porosity in the NCLS experiment towards the end could potentially be attributed to the clogging of certain pores by migrating calcite particles after detachment due to dissolution of some of the matrix.

For the experiment HCHS, macroporosity of the top half of the sample first slightly decreased and then this decreased macroporosity was nearly maintained until the end of the experiment, where a slight increment was observed (Fig. 3b). Luquot et al. (2014) has also observed similar decrement in the macroporosity for the acids with lower corrosiveness (i.e., less strong undersaturation). They noted that the acids with lower reactive strength attack the microporosity of the grain and resultant small particles clog the macropores. The change in macroporosity obtained from XMT images does not resolve such changes in microporosity. Therefore, changes in the microporosity of the sample were investigated through changes in grey volume in the full samples between beginning and end of the experiment (SI Section S5.2). For the same sections of the sample (i.e., cropped sample length) of this experiment, we observed that the total change in the grey volume (i.e.,

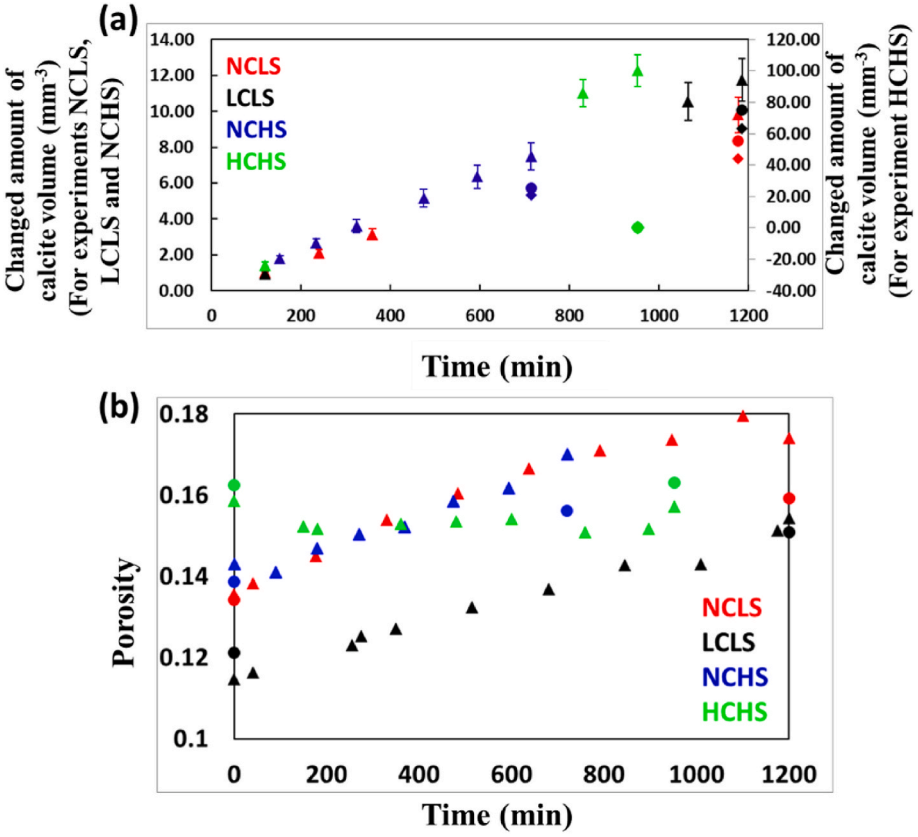

Fig. 3. (a) Cumulative changes in the solid calcite volume calculated from effluent analysis (triangle) and using XMT images (circle, full sample length and diamond, cropped sample length) for experiments NCLS, LCLS, NCHS (left-hand vertical axis) and HCHS (right-hand vertical axis). (b) temporal evolution of the macroporosity calculated from XMT images (circle, cropped sample length and triangle, half sample length) for all four experiments.

microporosity + macroporosity) was 3.3×10^{-9} m^3 as compared to the segmented volume (i.e., macroporosity) of a value of 0.16×10^{-9} m^3 (Fig. S14: semi quantitative). This suggests that the inflow solution HCHS had dissolved more sub-resolution calcite matrix and the detached fine grains accumulated in the macropores (cf. Luquot et al., 2014).

Fig. 4 provides a vertical profile of porosity along the direction of the flow. Each data point was obtained by averaging using a moving windows including 30 consecutive 2D slices (i.e., corresponding to 0.18 mm). Comparison of the vertical porosity profile of the samples from the initial and final time steps of the dissolution experiment unveiled the following information:

Firstly, for experiment NCLS, we observed a strong deviation of evolved porosity distribution along the flow path compared to initial porosity distribution whereas, for experiment LCLS and NCHS, evolved porosity distribution was similar to initial porosity distribution (Fig. 4a). This is caused by the difference in reactive strength of the injecting fluid, as also discussed Section 3.2.1.

Next, we observed that solution NCLS created maximum porosity changes in the first 2 mm part of the sample whereas for solution LCLS, the effective depth of reaction front (i.e., corresponds to a porosity difference (new porosity (%) - old porosity (%)) of more than 3%) was around 5 mm (Fig. 4b). In the case of solution NCHS, the top 3 mm part of the sample experienced an average of 3% porosity change. The depth of penetration of the reaction front is related to the amount of fluid buffering. Fluid buffering is a result of a complex interplay of initial reactive strength of the injecting fluid and transport time scale (e.g., Agrawal et al., 2020; Gray et al., 2018; Molins et al., 2014). Section 3.1.4 explores this relationship between reaction and transport time scale for an individual experiment. For experiments NCLS, LCLS, and NCHS, the whole sample showed positive porosity changes, whereas, for experiment HCHS, the top part of the sample showed negative porosity changes (Fig. 4b). It is worth noting that for experiment HCHS, % macroporosity difference is less than 0.5% and that dissolution in micropores played an important role. Alternatively, the SI values obtained with our generalized Pitzer model may be inaccurate (Harvie and Weare, 1980; Felmy and Weare, 1986), and locally calcite supersaturation may have occurred, leading to the observed pore clogging/-porosity decrease.

Note that, due to the constraints with the data acquisition as mentioned in Section 2.2, bulk porosity for the first- and last-time steps of the experiment was calculated from the data of the full sample (Fig. 3b). However, porosity for the intermediate time steps was calculated from the data of half-length sample i.e., part of the sample near the injection point. The difference between porosity data of these two samples size at time $t = 0$ denotes the initial heterogeneity of the samples (Fig. 4a) whereas, the difference at the end of the experiment is a result of dissolution heterogeneity along the direction of flow (Fig. 4b).

3.1.4. *Reaction rate and dimensionless numbers*

Time-lapse XMT scans of the sample enabled monitoring of the macroporosity of the sample as the experiment progressed. This porosity was utilized to obtain the changed amount of calcite mass to calculate the evolution of the average reaction rate over the course of the experiments. Fig. 5a shows the evolution of the average reaction rate for all four experiments. Fig. 6 shows the vertical profile of the local reaction rate calculated from the XMT images of the full sample obtained at the beginning and the end of the experiment.

We observed that the addition of the Ca^{2+} ions in the inflow solution decreased the calcite dissolution rate (NCLS vs LCLS and NCHS vs HCHS in Figs. 5a and 6). For example, at 40 min, the average dissolution rate corresponding to the NCLS solution was 47.3% higher than the solution

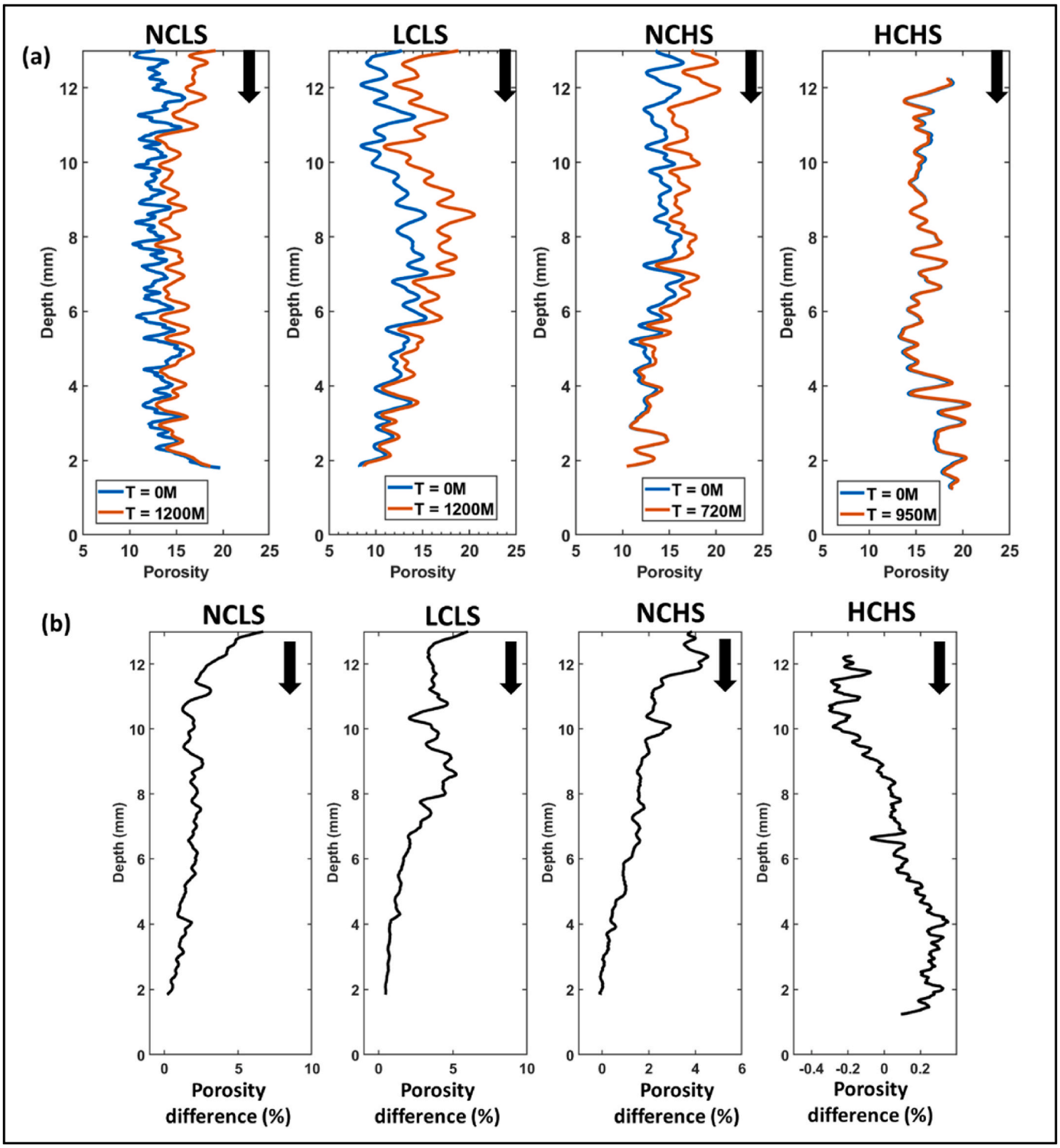

Fig. 4. Porosity changes in all four experiments showing (a) the slice-averaged porosity values (%) along the sample, and (b) difference between porosity values (%). The vertical profiles corresponded to the XMT images of the cropped sample length at the beginning and the end of experiment. In order to increase the visibility, only a part of the vertical profile (i.e., from 1.8 till 12.5 mm) is shown. Fig. S15 shows the full vertical profile (i.e., from 1.8 mm till 13.5 mm). Black arrow indicates the flow direction. Note the different x-axis ranges utilized for panel (b). Note that flow was established from bottom to top of the sample and all presented images are upside down.

LCLS. Similarly, the solution NCHS (i.e., no Ca^{2+} ions and high salinity) also showed a higher average dissolution rate as compared to the solution HCHS (i.e., 337 $\times$ 10^{-3} mol dm^{-3} Ca^{2+} ions and high salinity). In the past, several studies have shown such inhibitory impact of the Ca^{2+} ions over the calcite dissolution kinetics (Buhmann and Dreybrodt, 1987; Sjöberg and Rickard, 1985).

We observed that the dissolution rate of macroporosity at the sample inlet for solution NCHS was approximately 54% less than solution NCLS (refer to Fig. 6). Additionally, the mean dissolution rate of macroporosity, calculated over half the sample length, was found to be lower

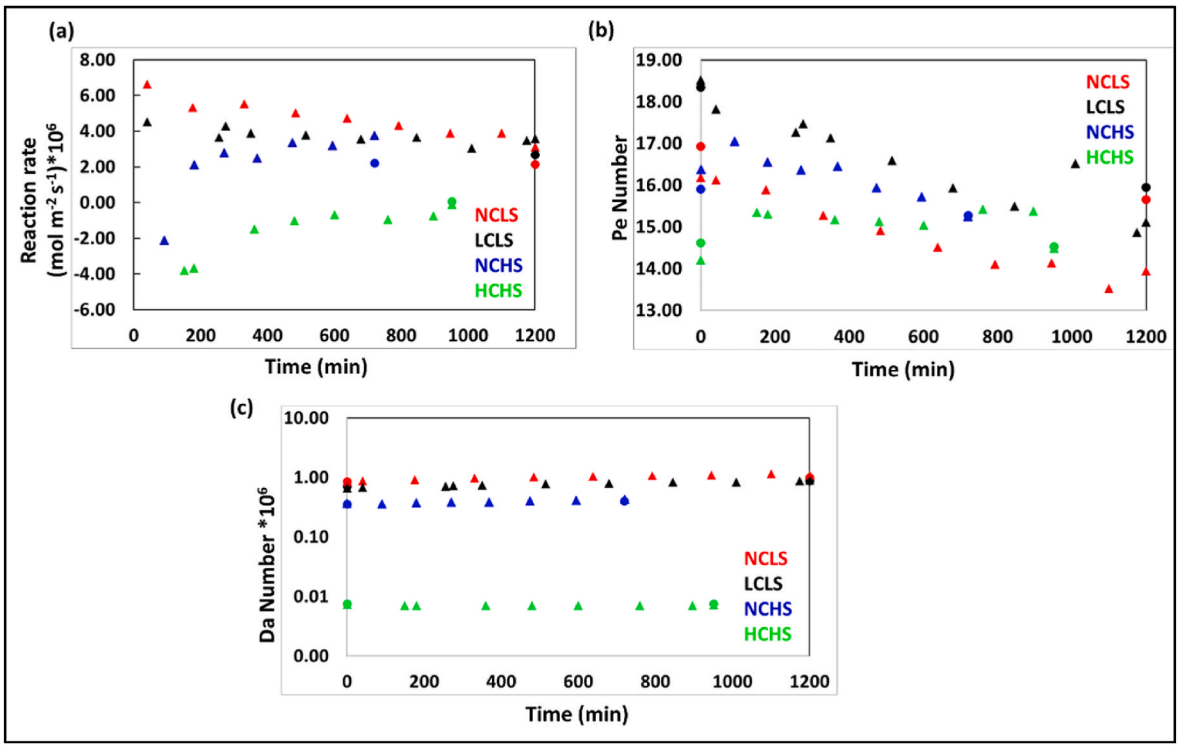

Fig. 5. Temporal evolution of (a) the average reaction rate based on Equation 6, (b) *Pe* Number, and (c) *Da* number, calculated from XMT images (circle, cropped sample length and triangle, half sample length).

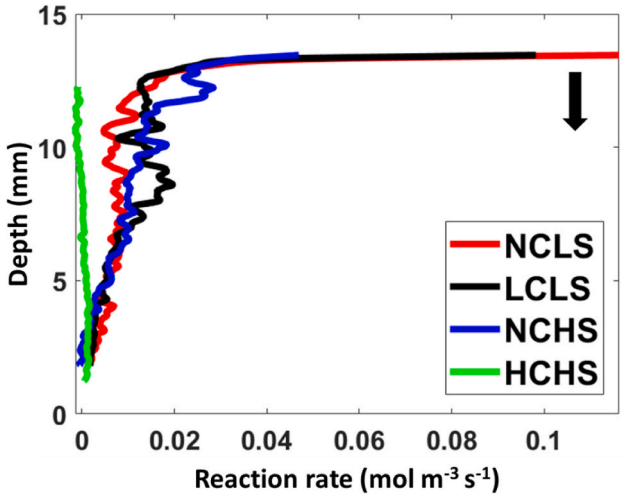

Fig. 6. The full vertical profiles of the slice-averaged dissolution rate for all four experiments calculated using Equation (7). The black arrow indicates the flow direction.

in experiment NCHS compared to NCLS (see Fig. 5a). Prior effluent analysis revealed higher outflow Ca2+ concentrations in experiment NCHS than in NCLS (Fig. 1a). A plausible justification is the conflicting impacts of salinity on the dissolution rate and the solubility of calcite. In saline solutions, the dissolution rate might be hindered, but the solubility of calcite might be enhanced. Consequently, saline solutions, despite exhibiting diminished macroporosity-based dissolution rates near the sample inlet, were able to dissolve more calcite across the entire sample length before reaching equilibrium with calcite. Another possible explanation is that a higher dissolution rate in microporosity regions in the NCHS experiment compared to NCLS experiment is currently not reflected in the calculated dissolution rates.

The *Pe* number for all four experiments was greater than one, indicating advection-controlled transport regimes such that the rate of renewal of the fluid inside pore space of the sample was dominated by advection (Fig. 5b). For all experiments, the *Da* number was less than 1.0. This suggests that the dissolution conditions in the sample were reaction-limited (Fig. 5c) as the time scale of advection is shorter than that of dissolution reaction. As the experiment progressed, we observed a decrease in the *Pe* number. This is because wormholes are dominantly responsible for porosity changes and average pore size did not increase by the same proportion as porosity increased.

For the studied reaction-controlled dissolution regime, this decrease of the *Pe* number also contributes to a decrement in the average dissolution rate (Fig. 5a). This impact of the temporal evolution of the *Pe* number over the average dissolution rate was much clearer in experiment NCLS compared to LCLS and NCHS experiments.

3.2. Evolution of the dissolution structure

All four experiments were performed with the same injection rate and on samples from the same rock type with very comparable pore structure (Fig. S11). Therefore, as expected, the reactive strength of the injecting solutions was directly reflected by the *Da* number. The *Da* number is highest for experiment NCLS, then LCLS, NCHS, and HCHS. Previously, the control of the *Da* number on the dissolution patterns has been investigated through both experimental and numerical studies (Fredd and Fogler, 1998; Golfier et al., 2002; Hoefner and Fogler, 1988; Luquot et al., 2014; Maheshwari et al., 2013). Table 2 provides overview of the dissolution patterns observed in the previous studies. In the next sections, we discuss the qualitative and quantitative aspects of the dissolution patterns developed in each experiment.

3.2.1. Dissolution structures in experiments NCLS, LCLS and NCHS

Experiment NCLS was performed with a solution that has low salinity, devoid of Ca^{2+} ions. This injected solution initiated the dissolution with an effective reaction rate of a magnitude of 7×10^{-6} mol m^{-2}

Table 2
Overview of the dissolution pattern observed in the previous studies.

Sample rock	*Pe*	Convective Da	Type of Dissolution	Reference
NaCl Salt grains packed porous media	8.32×10^{-4}	120	Face dissolution	Golfier et al. (2002)
	4.14×10^{-3}	24	Conical wormhole	
	1.66	6.01×10^{-2}	Dominant wormhole	
	83.2	1.2×10^{-3}	Ramified wormhole	
	832	1.2×10^{-14}	Uniform dissolution	
Oolitic grainstone from the Lusitanian Basin	0.2	$0.1\text{-}1 \times 10^{-4}$	Dominant wormhole and uniform dissolution	Luquot et al. (2014)
Ketton carbonate rock	9	0.5	Dominant wormhole	Gray et al. (2018)
Ketton carbonate rock	2100	2.8×10^{-5}	Uniform dissolution	Menke et al. (2015)
Ketton carbonate rock	14–19	7.28×10^{-9} - 8.53×10^{-7}	Dominant wormhole – Uniform dissolution	This study

s^{-1} (Fig. 5a). Addition of a small amount Ca^{2+} ions (experiment LCLS), lowered initial effective reaction rate to 4×10^{-6} mol m^{-2} s^{-1} (Fig. 5a). In the experiment NCHS, injection of a saline solution that did not contain Ca^{2+} ions, caused a lower dissolution rate than in experiments NCLS and LCLS (Figs. 5a and 6).

The time-lapse scanning of the pore space allowed a qualitative analysis of the temporal evolution of the dissolution structures in these experiments. In experiment NCLS, it was noted that dissolution was remarkably uniform in the radial direction during the initial 40 min (Fig. 7a), indicating that the initial phase of dissolution was primarily influenced by fluid acidity rather than the sample's initial pore structure (Fig. 7a). Such difference between the modified porosity and the initial porosity was also clear in the vertical porosity profiles provided in Fig. 4a. The radially homogeneous dissolution occurred in the first ~2 mm of the flow path, after which selective dissolution paths continued further along the flow direction (Fig. 7a). This development of dissolving channels was most likely guided by the initial heterogeneity and structure of the sample. Conversely, for experiments with lower Da numbers (i.e., LCLS and NCHS the formation of the dissolution structure was more significantly influenced by the heterogeneous pore structure of the sample, as contrasted with experiment NCLS (Fig. 7b–c, and 4a). For example, in the experiment LCLS, after 40 min of acid injection, dissolution created sparsely localized flow channels (Fig. 7b). From the scans of the half sample length, we observed that the sample's pore space evolved into several conducting channels. The trajectories and length of these channels were established within a certain experiment duration (i.e., 484 min in experiment NCLS, 255 min in experiment LCLS and 369 min in experiment NCHS) while the diameter of channel continued to grow (Fig. 7 and S16). From the scan of the full sample, which was acquired at the end of the experiment (i.e., 1200 min for the experiments NCLS and LCLS; 720 min for the experiment NCHS), we observed that most of these channels did not develop much beyond the half sample length that was scanned during the experiment (Fig. 8). In the experiment NCLS, two of the channels extended over the full length of the sample, while in the experiments LCLS and NCHS, only one such dominant channel was formed (Fig. 8).

Next, through skeleton analysis, we characterized and quantified final form of the dissolution structures in these three experiments (Fig. S17; Table S2). The quantification was based on attributes derived from the individual segments of the channels and side branches: the length (sum of the segment length), radius (radius of the segments) and mean radius (average of the segment radius).

The evolution of the dissolution structures also indicates that the less reactive injecting solutions (i.e., higher Ca^{2+} and/or salt concentration) resulted in localization of the channels. This was evident from the decreasing number of inlet nodes (where the number of inlet nodes shows unique/main flow channels) with the decreasing Da number (Table S2). All the channels originating from the inlet nodes were divided into three categories based on their lengths (Figs. S18–S20; Table S2). Fig. S21 shows the histogram of the channel lengths for experiments NCLS, LCLS and NCHS. We observed that in the experiment NCLS, two dominant channels of a length ~14 mm were formed. In contrast, in the experiments LCLS and NCHS, only one dominant channel of the length of 12.30 and 10.28 mm, respectively, was formed.

The impact of the reactivity of the injected solution on the starting diameter of the channel was also observed (i.e., in the vicinity of the sample inlet). For example, in the experiment NCLS, the starting diameter of two of the category 1 channels was larger than 0.6 mm while, in the experiments LCLS, the starting diameter of both of the category 1 channels was smaller than 0.4 mm (Figs. S22a and b). Moreover, the *Da* number also represents the buffering of fluid as it moves along the sample (Agrawal et al., 2020). This is reflected in the vertical radius profile (i.e., in the direction of flow) of the channels. In the experiments LCLS and NCHS, the vertical radius profiles of the category 1 channels were more homogeneous than the experiment NCLS (Fig. S22).

Furthermore, in the experiment LCLS, for each category 1 channel, the number of side branches and the length of the side branches were significantly higher than the experiment NCLS (Table S2, Figure S23a-b and S24a-b). The increased ramification of dissolution channels with decreasing *Da* number has also been observed by Luquot et al. (2014). On the contrary, the dissolution pattern in the experiment NCHS developed with the least amount of ramification as evident from the least number of end nodes (Table S2, Fig. S23c).

3.2.2. *Experiment HCHS*

We observed that the presence of a high amount of Ca^{2+} ions lowered the effective dissolution rate by two orders of magnitude compared to experiment NCHS (Fig. 5a). As mentioned earlier, the macroporosity of the top part of the sample decreased throughout this experiment (Figs. 3b and 4). Fig. 9 presents the temporal evolution of the pore space where the locations of removed solid mass and of added solid mass are highlighted. As explained earlier, the injected HCHS was acidic and undersaturated with respect to the calcite and mixing calculations (performed in PHREEQC with default Pitzer database) showed that it is unlikely that mixing variable amounts of the HCHS solution with the equilibrated initial solution present in the sample can result in a composition that is supersaturated with respect to calcite. A possible explanation of the accumulated solid mass in the pore space is related to the dissolution of the microporous matrix, causing solid particles to detach from the matrix and migrate through the pore space. This is described by the so-called sugar lump model (Luquot et al., 2014). From the XMT image after 150 min of acid injection, we observed that small amounts of such displaced particles were uniformly distributed in the pore space (blue in Fig. 9). Dissolution of the microporous matrix was confirmed by grey value analysis of the images (Fig. S14; semi quantitative), which showed an increase in the sum of microporosity and macroporosity. From the scan of the full sample at the end of the experiment (Fig. 9c), we observed that the amount of clogging by displaced solid particles was higher closer to the inlet. This is consistent with most of the dissolution occurring closer to the inlet, also in the microporous domain, leading to more detachment and local displacement of particles. Alternatively, use of the default Pitzer model in PHREEQC for the calculation of the solution chemistry might have led to an overestimation of the undersaturation state of the inflow solution (Harvie and Weare, 1980; Felmy and Weare, 1986) and locally calcite supersaturation may have occurred, leading to the observed pore

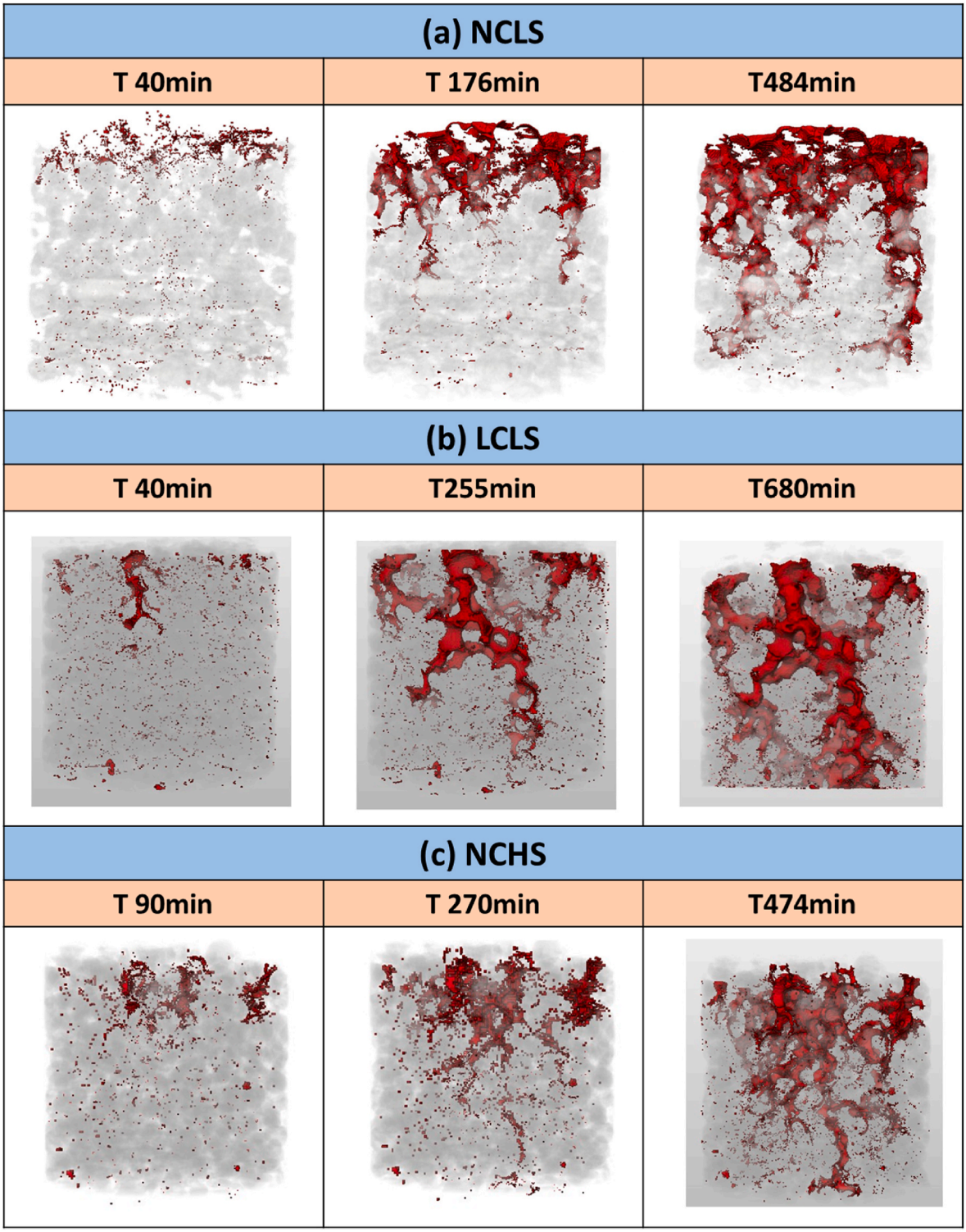

Fig. 7. Temporal evolution of the dissolution patterns in experiment (a) NCLS, (b) LCLS and (c) NCHS. XMT images of these samples at the remaining time steps are shown in Fig. S16.

clogging.

3.3. Evolution of transport properties

Dissolution patterns control permeability changes in the sample, which is related to the volume of acid injection required for wormhole breakthrough (PV_{BT}). One of the earlier definitions of wormhole breakthrough is when the permeability of the sample increases by a factor of 100 (Fredd and Fogler, 1998). The amount of acid required for a breakthrough is a function of the dissolution pattern, and therefore depends on *Pe* and *Da* numbers, which reflect the injection rate and the solution's corrosive nature (i.e., chemical reactivity, in the current case determined by salinity and calcium concentration). For example, face dissolution will require higher volumes of acid to attain a certain permeability increment than wormholes.

Fig. S26 shows the temporal evolution of permeability calculated

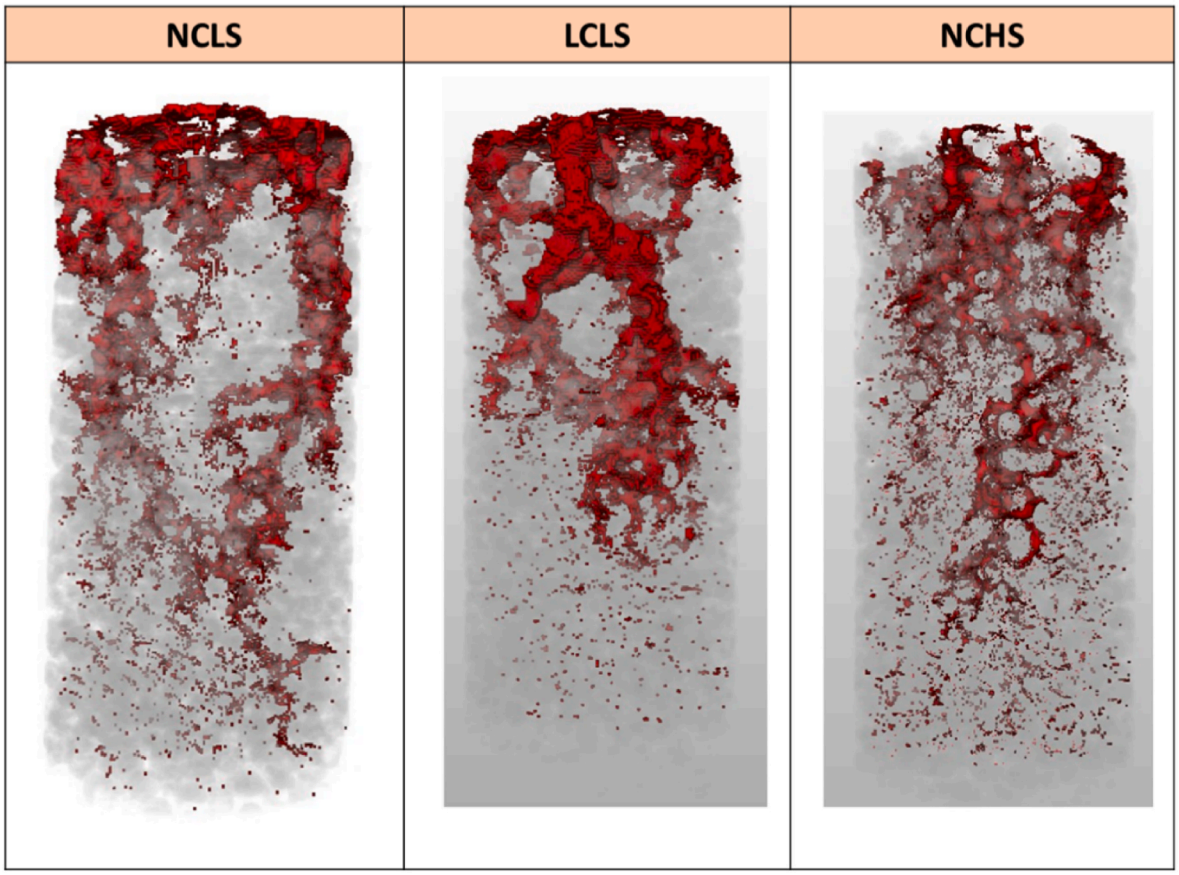

Fig. 8. Final form of the dissolution patterns in experiments NCLS, LCLS and NCHS. Note that the duration of experiments NCLS, LCLS and NCHS was 1200, 1200 and 720 min.

from both the pore network model and direct numerical simulation during all four experiments. For all experiments, both methods yielded a similar amount of permeability change - i.e., a noticeable permeability increment in the experiments NCLS, LCLS, and NCHS, and no significant permeability change in experiment HCHS.

If we consider the definition of breakthrough from Fredd and Fogler (1998), none of the experiments in this study led to a breakthrough point (Fig. S27). The highest permeability increment corresponding to a factor of 7.9 and 5.8 was noted for experiment LCLS based on permeability values from the pore network model and direct numerical simulations, respectively. We observed that the injection of the same number of pore volumes resulted in the highest permeability increment for experiment LCLS and lowest for experiment HCHS (Fig. S27). This indicates that the dissolution pattern formed in experiment LCLS is optimal, just as the *Da* number of this experiment is ideal among all four experiments.

The volume of acid required for a breakthrough was calculated through the extrapolation of the direct numerical simulation-based permeability response curve as shown in Fig. S27. Fig. 10 shows the distribution of PV_{BT} as a function of *Da* number. As expected for experiment LCLS, the lowest amount of pore volumes was required to achieve an increase in permeability by a factor of 100. This suggests that the increasing amount of salinity and Ca^{2+} concentration of the injecting solution results in an increase in the number of acid pore volumes required for changing the permeability.

Fig. 11 shows the changes in permeability as a function of porosity for all four experiments. In the past, several experimental and modelling studies have used the simplified version of Kozeny -Carman relation i.e., a power-law relation as $k \sim \phi^n$, to relate the permeability changes with the evolving porosity of the sample (e.g. Bernabé et al., 2003; Luquot et al., 2014; Luquot and Gouze, 2009; Nogues et al., 2013; Pereira Nunes et al., 2016). The exponent n is a function of the initial porous medium properties and the processes which cause the changes in the pore structure. A higher value of n results in higher permeability change with small porosity changes. In the past, a number of experimental studies have reported a range of values for exponent n, corresponding to the dissolution pattern developed in different types of carbonate rocks (e.g., Menke et al., 2015; Luquot and Gouze, 2009; Luquot et al., 2014). For example, for a uniformly dissolving Ketton carbonate, Menke et al. (2015) obtained a value of 5.16 while Luquot and co-workers (2009, 2014) found values of 0.29 and 0.32 corresponding to the development of homogeneous dissolution pattern in Oolitic Limestone. To calculate the exponent, we used half sample length-based porosity and permeability values instead of cropped sample length. This is because, for curve fitting, we had multiple data points from the half sample length while only two data points from the cropped sample length. We obtained the lowest value of n corresponding to the uniform dissolution patterns in the experiment HCHS (Fig. 10). For the variety of wormholes formed in the other three experiments, we noted that the value of exponent n lies between 9 and 11 (Fig. 11). Luquot et al. (2014) also obtained a high value of $n = 7.07$ corresponding to the formation of dominant wormholes. Since the initial porous medium structures for the various experiments presented here was similar (Fig. S11), this wide range of n values noted in this study most likely reflects the composition of the injected solution, and therefore Da number. Additionally, for all experiments except LCLS, we observed an alignment in the porosity-permeability trend from half sample length and cropped sample length datasets. In the case of experiment LCLS, porosity-permeability changes in cropped sample length indicate a lower exponent compared to in the half sample length. This is due to the initial heterogeneity of sample K2 along the flow direction as also

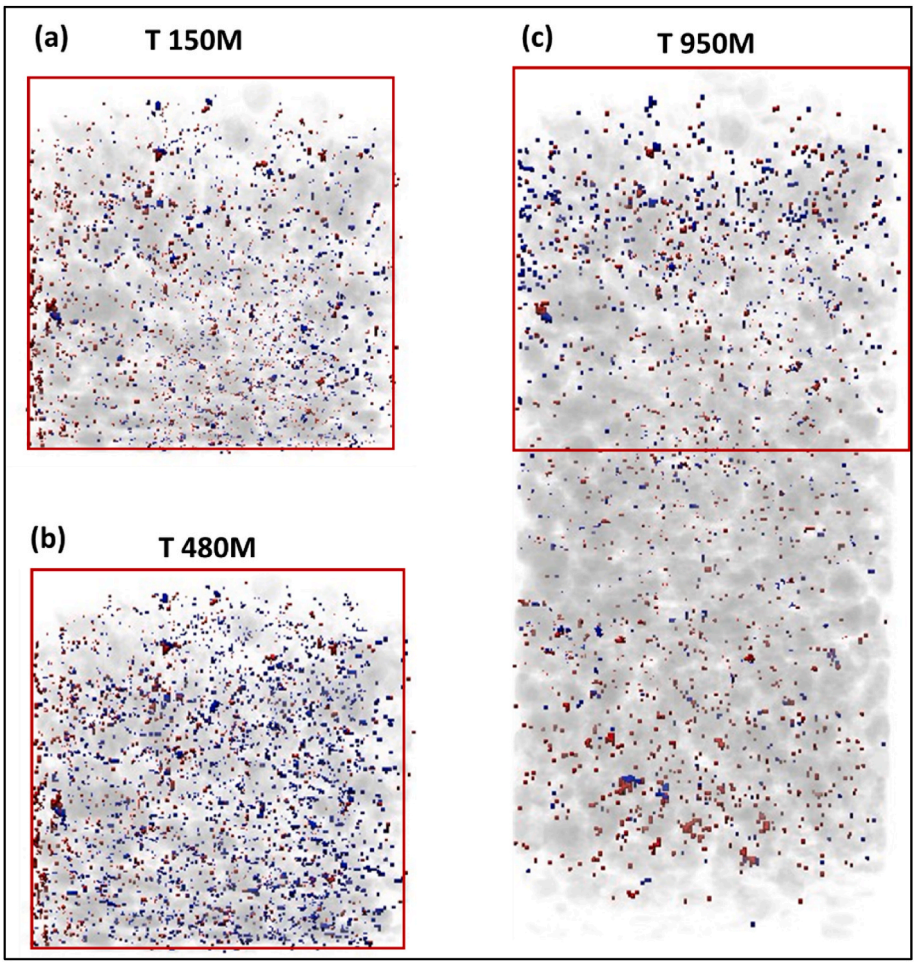

Fig. 9. Temporal evolution of the pore space in the experiment HCHS. Red colour highlights the locations from where the solid mass was removed. Blue colour highlights the locations where the solid mass was added. XMT images of this sample at other time steps are shown in Fig. S25. Note that red coloured box shown in plot (c) indicates the volume imaged in plots (a) and (b).

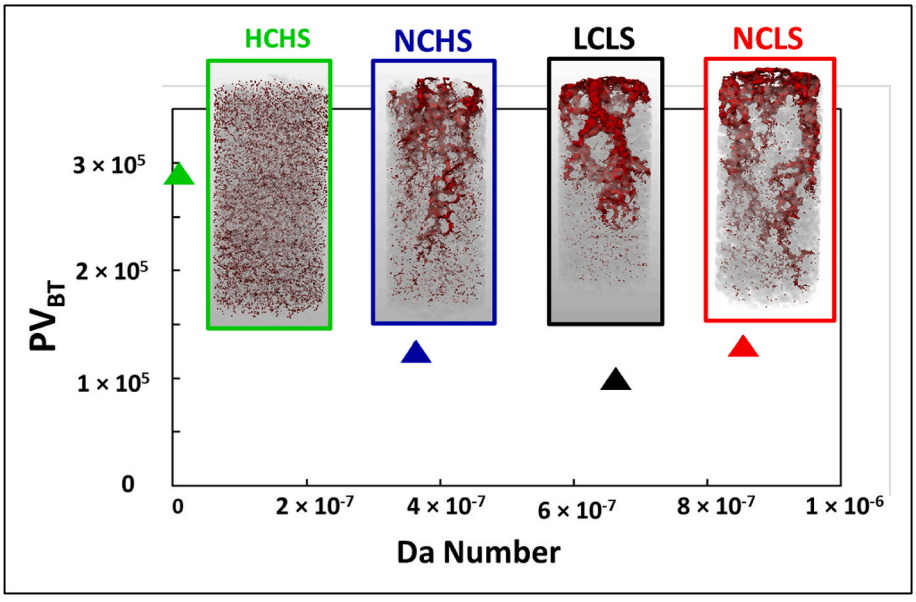

Fig. 10. The expected number of pore volumes to obtain a full breakthrough curve at different *Da* number. Note that direct numerical simulation permeability, k_{DNS}, was used for the calculation of PV_{BT}.

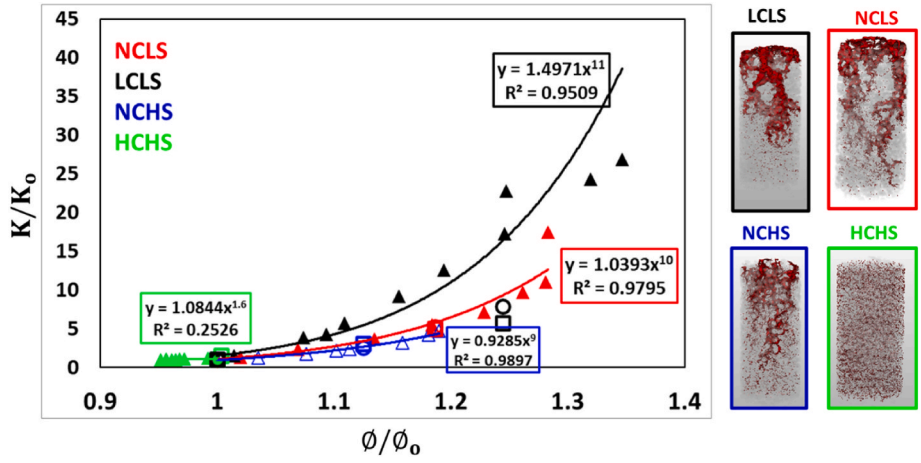

Fig. 11. Permeability-porosity relationships for the four experiments. Circle and triangle markers show PNM results for pore network extracted from cropped sample length XMT images and half sample length XMT images, respectively. Square markers show DNS results for the cropped sample length XMT images. Note that the porosity-permeability relationship is obtained by fitting a power-law curve in the PNM based permeabilities of half sample length datasets.

indicated by the difference in the macroporosity values at t = 0 (Fig. 3b). It cannot be ruled out completely that subtle differences in the initial pore structure of different samples affected the distinct pore structures that evolved during the dissolution experiment. Nevertheless, our results strongly suggest that lower dissolution rates at the sample inlet (experiment LCLS) favor the rapid formation of localized channels compared to solutions with a higher reactivity (experiment NCLS). It can therefore be concluded that adjusting the chemistry of the injecting fluid creates an interplay between reaction and transport time scales that guide a dissolving porous medium to evolve into different pore structure. This suggests that precaution should be taken in the generalization of a single porosity-permeability model for a range of reservoirs containing formation water of different salinities. Potentially, the impact of Ca^{2+} concentration and salinity can be implemented in the derivation of porosity-permeability models to improve their predictability.

4. Conclusions

In this study, we employed time-lapse imaging to explore the dissolution of Ketton limestone across four samples under uniform flow conditions but varying reactive conditions, imposed by the composition of injected brine. The imaging highlighted the different stages in the evolution of dissolution patterns, governed by the Da number—subsequently influenced by salt concentration. XMT scans at sequential time steps showed the constant interplay between changing porosity and permeability of the samples and the evolution of flow patterns and average reaction rates.

Our observations highlighted the profound influence of brine composition on alterations in porosity and permeability. The concentration of calcium ions and sodium chloride in the injecting solution emerged as determinants of the calcite dissolution rate, both displaying substantial inhibitory effects. Solutions with minimal salinity and no calcium ions resulted in the most effective calcite dissolution rate, with predominant dissolution near the sample inlet and relatively less along the flow path, creating wormholes with vertically diverse radius profiles. In contrast, solutions with low calcium concentration led to the formation of selective dissolution paths, yielding more uniformly structured wormholes with extensive ramifications. High salt and calcium concentrations significantly decreased dissolution rates, with minimal and uniformly distributed dissolution mainly within the micropore space.

In essence, elevated levels of salt and Ca^{2+} ions induced a reaction-limited dissolution regime, maintaining the solution's corrosive properties over extensive penetration depths, resulting in homogeneous dissolution. Conversely, reducing salt and Ca^{2+} concentrations shifted the system towards a transport-dominated dissolution regime, leading to non-uniform dissolution, as the formation of wormholes became evident due to the positive feedback between increased permeability and heightened mass transfer rates (Golfier et al., 2002).

The obtained range of Kozeny-Carman exponents, reflecting the relationship between rock permeability and porosity evolution, was broad, attributed to the variability in the corrosiveness of the injected solutions. To summarize, diverse combinations of salinity and Ca^{2+} concentrations in the injected solution could alter dissolution from a disseminated and microporous regime to a wormhole regime, resulting in variations in the porosity-permeability relationship. It is important to acknowledge the limitations in this study, such as the absence of lab measurements of porosity and permeability data, leading to uncertainties in quantifying initial pore structures. Addressing these constraints through extended experimental or modelling methodologies will pave the way for enhanced insights in this research direction.

Declaration of competing interest

The authors declare that they have no known competing financial interests or personal relationships that could have appeared to influence the work reported in this paper.

Data availability

Data will be made available on request.

Acknowledgements

The research work of P.A., M.W. and A.R is part of the Industrial Partnership Programme i32 Computational Sciences for Energy Research that is carried out under an agreement between Shell and the Netherlands Organization for Scientific Research (NWO). M.W. has received funding from the European Research Council (ERC) under the European Union's Horizon 2020 research and innovation programme (grant agreement No. [819588]). The XMT experiments in this work were performed at Ghent University's Centre for X-ray Tomography (UGCT), a Centre of Expertise funded by the Ghent University Special Research Fund (BOF-UGent) under grant BOF.EXP.2017.007. TB, AM and VC received funding from the Research Foundation–Flanders (FWO) under project grant G051418N. TB is a postdoctoral fellow of the Research Foundation-Flanders (FWO) and acknowledges its support under Grant 12X0919N. We also thank two anonymous reviewers for

their insightful comments, which greatly improved the work.

Appendix A. Supplementary data

Supplementary data to this article can be found online at https://doi.org/10.1016/j.apgeochem.2023.105835.

References

Akbar, M., Vissapragada, B., Alghamdi, A.H., Allen, D., Herron, M., et al., 2000. A snapshot of carbonate reservoir evaluation. Oilfield Rev. 12, 20–40.

Agrawal, P., Raoof, A., Iliev, O., Wolthers, M., 2020. Evolution of pore-shape and its impact on pore conductivity during CO2 injection in calcite: single pore simulations and microfluidic experiments. Adv. Water Resour. 136.

Al-Khulaifi, Y., Lin, Q., Blunt, M.J., Bijeljic, B., 2017. Reaction rates in chemically heterogeneous rock: coupled impact of structure and flow properties studied by X-ray microtomography. Environ. Sci. Technol. 51, 4108–4116.

Anabaraonye, B.U., Crawshaw, J.P., Trusler, J.P.M., 2019. Brine chemistry effects in calcite dissolution kinetics at reservoir conditions. Chem. Geol. 509, 92–102.

Aslannejad, H., Fathi, H., Hassanizadeh, S.M., Raoof, A., Tomozeiu, N., 2018. Movement of a liquid droplet within a fibrous layer: direct pore-scale modeling and experimental observations. Chem. Eng. Sci. 191, 78–86.

Bedram, A., Moosavi, A., 2011. Droplet breakup in an asymmetric microfluidic T junction. Eur. Phys. J. E 34.

Bernabé, Y., Mok, U., Evans, B., 2003. Permeability-porosity relationships in rocks subjected to various evolution processes. Pure Appl. Geophys. 160, 937–960.

Boone, M.A., De Kock, T., Bultreys, T., De Schutter, G., Vontobel, P., Van Hoorebeke, L., Cnudde, V., 2014. 3D mapping of water in oolithic limestone at atmospheric and vacuum saturation using X-ray micro-CT differential imaging. Mater. Char. 97, 150–160.

Buhmann, D., Dreybrodt, W., 1987. Calcite dissolution kinetics in the system H_2O-CO_2-$CaCO_3$ with participation of foreign ions. Chem. Geol. 64, 89–102.

Bultreys, T., Boone, M.A., Boone, M.N., De Schryver, T., Masschaele, B., Van Hoorebeke, L., Cnudde, V., 2016. Fast laboratory-based micro-computed tomography for pore-scale research: illustrative experiments and perspectives on the future. Adv. Water Resour. 95, 341–351.

Daccord, G., Lenormand, R., Liétard, O., 1993. Chemical dissolution of a porous medium by a reactive fluid-I. Model for the "wormholing" phenomenon. Chem. Eng. Sci. 48, 169–178.

Elkhoury, J.E., Ameli, P., Detwiler, R.L., 2013. Dissolution and deformation in fractured carbonates caused by flow of CO2-rich brine under reservoir conditions. Int. J. Greenh. Gas Control 16, S203–S215.

Esteves, B.F., Lage, P.L.C., Couto, P., Kovscek, A.R., 2020. Pore-network modeling of single-phase reactive transport and dissolution pattern evaluation. Adv. Water Resour. 145, 103741.

Felmy, A.R., Weare, J.H., 1986. The prediction of borate mineral equilibria in natural waters : application to Searles Lake. California 50, 2771–2783.

Finneran, D.W., Morse, J.W., 2009. Calcite dissolution kinetics in saline waters. Chem. Geol. 268, 137–146.

Fredd, C.N., Fogler, H.S., 1998. Influence of transport and reaction on wormhole formation in porous media. SPE J. 44, 1933–1949.

Garcia-Rios, M., Luquot, L., Soler, J.M., Cama, J., 2015. Influence of the flow rate on dissolution and precipitation features during percolation of CO_2-rich sulfate solutions through fractured limestone samples. Chem. Geol. 414, 95–108.

Gledhill, D.K., Morse, J.W., 2006. Calcite dissolution kinetics in Na-Ca-Mg-Cl brines. Geochem. Cosmochim. Acta 70, 5802–5813.

Golfier, F., Zarcone, C., Bazin, B., Lenormand, R., Lasseux, D., Quintard, M., 2002. On the ability of a Darcy-scale model to capture wormhole formation during the dissolution of a porous medium. J. Fluid Mech. 457, 213–254.

Gray, F., Anabaraonye, B., Shah, S., Boek, E., Crawshaw, J., 2018. Chemical mechanisms of dissolution of calcite by HCl in porous media: simulations and experiment. Adv. Water Resour. 121, 369–387.

Gutjahr, A., Dabringhaus, H., Lacmann, R., 1996. Studies of the growth and dissolution kinetics of the CaCo3 polymorphs calcite and aragonite I. Growth and dissolution rates in water. J. Cryst. Growth 158, 296–309.

Hanor, J.S., 1994. Origin of saline fluids in sedimentary basins. Geol. Soc. Spec. Publ. 78, 151–174.

Harvie, C.E., Weare, J.H., 1980. The prediction of mineral solubilities in natural waters: the NaKMgCaClSO4H2O system from zero to high concentration at 25° C. Geochem. Cosmochim. Acta 44, 981–997.

Hoefner, M.L., Fogler, H.S., 1988. Pore evolution and channel formation during flow and reaction in porous media. AIChE J. 34, 45–54.

Hoefner, M.L., Fogler, H.S., Stenius, P., Sjoblom, J., 1987. Role of acid diffusion in matrix acidizing of carbonates. JPT, J. Pet. Technol. 39, 203–208.

Luquot, L., Gouze, P., 2009. Experimental determination of porosity and permeability changes induced by injection of CO_2 into carbonate rocks. Chem. Geol. 265, 148–159.

Luquot, L., Rodriguez, O., Gouze, P., 2014. Experimental characterization of porosity structure and transport property changes in limestone undergoing different dissolution regimes. Transport Porous Media 101, 507–532.

Maheshwari, P., Ratnakar, R.R., Kalia, N., Balakotaiah, V., 2013. 3-D simulation and analysis of reactive dissolution and wormhole formation in carbonate rocks. Chem. Eng. Sci. 90, 258–274.

Meile, C., Tuncay, K., 2006. Scale dependence of reaction rates in porous media. Adv. Water Resour. 29, 62–71.

Menke, H.P., Bijeljic, B., Andrew, M.G., Blunt, M.J., 2015. Dynamic three-dimensional pore-scale imaging of reaction in a carbonate at reservoir conditions. Environ. Sci. Technol. 49, 4407–4414.

Menke, H.P., Bijeljic, B., Blunt, M.J., 2017. Dynamic reservoir-condition microtomography of reactive transport in complex carbonates: effect of initial pore structure and initial brine pH. Geochem. Cosmochim. Acta 204, 267–285. https://doi.org/10.1016/j.gca.2017.01.053.

Molins, S., Trebotich, D., Yang, L., Ajo-Franklin, J.B., Ligocki, T.J., Shen, C., Steefel, C.I., 2014. Pore-scale controls on calcite dissolution rates from flow-through laboratory and numerical experiments. Environ. Sci. Technol. 48, 7453–7460.

Morse, J.W., Mackenzie, F.T., 1990. Geochemistry of Sedimentary Carbonates. Elsevier, Amsterdam, p. 707.

Nan, Z., Shi, Z., Yan, B., Guo, R., Hou, W., 2008. A novel morphology of aragonite and an abnormal polymorph transformation from calcite to aragonite with PAM and CTAB as additives. J. Colloid Interface Sci. 317, 77–82. https://doi.org/10.1016/j.jcis.2007.09.015.

Nogues, J.P., Fitts, J.P., Celia, M.A., Peters, C.A., 2013. Permeability evolution due to dissolution and precipitation of carbonates using reactive transport modeling in pore networks. Water Resour. Res. 49, 6006–6021.

Panga, M.K.R., Ziauddin, M., Balakotaiah, V., 2005. Two-scale continuum model for simulation of wormholes in carbonate acidization. AIChE J. 51, 3231–3248.

Parkhurst, D., Appelo, C., 2013. Description of Input and Examples for PHREEQC Version 3—A Computer Program for Speciation, Batch-Reaction, One-Dimensional Transport, and Inverse Geochemical Calculations.

Pereira Nunes, J.P., Blunt, M.J., Bijeljic, B., 2016. Pore-scale simulation of carbonate dissolution in micro-CT images. J. Geophys. Res. B Solid Earth 121, 558–576.

Pokrovsky, O.S., Golubev, S.V., Schott, J., 2005. Dissolution kinetics of calcite, dolomite and magnesite at 25 °C and 0 to 50 atm pCO_2. Chem. Geol. 217, 239–255.

Raoof, A., Nick, H.M., Wolterbeek, T.K.T., Spiers, C.J., 2012. Pore-scale modeling of reactive transport in wellbore cement under CO2 storage conditions. Int. J. Greenh. Gas Control 11, 67–77.

Schlumberger, 2019. Technical challenges—carbonate reservoirs. https://www.slb.com/technical-challenges/carbonates.

Soulaine, C., Roman, S., Kovscek, A., Tchelepi, H.A., 2017. Mineral dissolution and wormholing from a pore-scale perspective. J. Fluid Mech. 827, 457–483.

Sjöberg, E.L., Rickard, D.T., 1985. The effect of added dissolved calcium on calcite dissolution kinetics in aqueous solutions at 25°C. Chem. Geol. 49, 405–413.

Yoo, H., Kim, Y., Jang, H., Lee, J., 2021. Propagation characteristics of optimum wormhole in carbonate matrix acidizing using micro X-ray CT imaging. J. Pet. Sci. Eng. 196, 108010.